Nanoscale

RSC Publishing

PAPER

Morphological transformation of hematite nanostructures during oxidation of iron

Cite this: *Nanoscale*, 2013, **5**, 7581

Lu Yuan,[a] Rongsheng Cai,[b] Joon I. Jang,[c] Wenhui Zhu,[a] Chao Wang,[b] Yiqian Wang*[b] and Guangwen Zhou*[a]

Received 4th April 2013
Accepted 18th June 2013

DOI: 10.1039/c3nr01669b

www.rsc.org/nanoscale

Oxidation of metals usually results in the formation of an oxide nanostructure with poorly controlled growth morphologies. By employing a simple mechanical approach that uses sandblasting to modify the surface roughness of iron substrates, we demonstrate that the morphologies of hematite (α-Fe_2O_3) nanostructures varying from the growth of one-dimensional nanowires to two-dimensional nanoblades can be achieved during the thermal oxidation of iron. Electron microscopy studies show that the effect of surface sandblasting is to effectively modify the oxide nucleation locations that define the growth shapes. The optical properties of hematite nanowires and nanoblades are examined for the demonstration of the morphology–property correlations.

1 Introduction

Metal oxides are among the most ubiquitous materials in nature. This abundance is dictated by the simple fact that oxides are typically more stable than their metallic counterparts in an oxidative environment, and many such materials can be formed by oxidation of metals in air. Metal oxides have provided a fundamental stepping-stone for the development of functional nanomaterials for applications ranging from semiconductors to insulators.[1] These exciting opportunities stem from the tunable functional properties (sensor, catalytic, electric, optical, *etc.*) of metal oxides *via* stoichiometry, coordination, and bonding of the constituent atoms that depend on the size, shape and dimensionality of the nanoscale systems.[2] In connection with this, it is of greatest practical importance to study oxidation of metals for the growth of metal oxide nanostructures, which can eliminate the need for many complex multistage processes of catalytic chemical synthesis of oxide nanostructures that involve many intermediaries. Due to its technical simplicity and large-scale growth capabilities, the growth of oxide nanostructures by thermal oxidation of metals has thus recently received intensive interest.[3] However, a significant challenge is the poor control over the growth morphologies of oxide nanostructures during the oxidation process, largely due to convolution of different processes involved in oxidation, including multi-phase oxide growth, coupling between growth stress and diffusion, and microstructure evolution.

Hematite (α-Fe_2O_3) is a nontoxic and the most stable iron oxide with a full set of functional properties. The use of α-Fe_2O_3 has been demonstrated in catalysis,[4] gas sensors,[5] water splitting,[6] dye solar cells,[7] magnetic storage media,[8] environmental protection,[9] and controlled drug delivery.[10] For instance, hematite has emerged as a strong candidate material for photoconversion of light to electric energy as it possesses a bandgap (E_g = 2.1 eV) that permits absorption of visible light.[11] It is essential that hematite crystallites should provide a high photoelectric yield efficiency. The growth of extended oxide nanostructures and, in particular, hematite nanostructures, is highly desired for these applications. Various α-Fe_2O_3 nanostructures have been reported by oxidation of Fe substrates to produce nanowires and nanobelts by controlling the oxidation conditions.[12] It was shown more recently that α-Fe_2O_3 nanowires, nanobelts, and platelets can be produced by introducing water vapor to the oxidation of shot-peening Fe substrates.[13] In this work we describe a simple approach that allows for tailoring the growth morphologies of hematite nanostructures during oxidation of iron. By exerting sandblasting onto Fe substrates, we show that a shape transition from the growth of α-Fe_2O_3 nanowires to α-Fe_2O_3 nanoblades can be achieved by increasing the surface roughness. These results shed light on the fabrication of unique hybrid morphology nanostructures *via* a simple way. These tunable growth morphologies may offer excellent opportunities to study the morphology–property correlations in nanostructured hematite, which is demonstrated in this work by examining the photoluminescence (PL) and nonlinear optical (NLO) properties of nanowires and nanoblades obtained from oxidation. The PL intensity and

[a]*Department of Mechanical Engineering & Multidisciplinary Program in Materials Science and Engineering, State University of New York, Binghamton, NY 13902, USA. E-mail: gzhou@binghamton.edu*

[b]*The Cultivation Base for State Key Laboratory, Qingdao University, Qingdao 266071, China. E-mail: yqwang@qdu.edu.cn*

[c]*Department of Physics, Applied Physics and Astronomy, State University of New York, Binghamton, NY 13902, USA*

high-order NLO susceptibilities are observed to show clear dependence on the oxide growth morphologies, which can be attributed to the surface effects. This may have broader implication for the aforementioned potential applications (*e.g.* heterogeneous catalysis, gas sensing) of nanostructured hematite because the fundamental processes governing these applications are mostly dominated by surface effects.

2 Experimental section

High-purity iron foils (99.99%) with a thickness of 0.25 mm obtained from Sigma-Aldrich are used in the oxidation experiments. The iron foils are first sandblasted by glass bead abrasives with a diameter range of 150–250 μm at the pressure of ~100 psi with different durations to modify the surface morphologies and surface roughness. The surface roughness of the sandblasted Fe samples is measured using an optical profiler (WYKO NT1100). The sandblasted samples are then thoroughly rinsed with deionized water followed by ultrasonication in acetone for 5 min. The cleaned Fe substrates are dried in N_2 and then placed on a substrate heater in a vacuum chamber and the sample temperature is monitored using a *K*-type thermocouple in contact with the substrate heater. The oxidation loading apparatus is large enough so that Fe specimens with different surface roughness can be loaded simultaneously and then oxidized under the same oxidation conditions. The oxidation chamber is first pumped to vacuum ($\sim 2 \times 10^{-6}$ Torr), and then filled with 300 mbar oxygen pressure (the purity of oxygen is 99.999%). The chamber is then sealed and the Fe samples are heated to 400 °C–600 °C at the rate of ~20 °C min^{-1} and oxidized at the temperature for different durations. It is then cooled down in the same oxygen atmosphere to room temperature at the rate of ~10 °C min^{-1}. Growth morphologies and crystal structures of the oxidized samples are examined using a field emission scanning electron microscopy (FEG-SEM, FEI Supra 55VP) and X-ray diffraction (XRD, PANalytical's X'Pert). Cross-sectional transmission electron microscopy (TEM) specimens are made from the oxidized Fe foils and analyzed using a JEOL JEM 2100F TEM that operated at 200 kV.

Both PL and NLO experiments are performed on the nanowire and nanoblade samples at room temperature. The pump beam is produced using an EKSPLA PL 2250 series diode-pumped picosecond Nd:YAG laser with a pulse width of 30 ps and a repetition rate of 50 Hz. An ESKPLA Harmonics Unit H400 is utilized along with an EKSPLA PG403-SH-DFG optical parametric oscillator to obtain a widely tunable coherent laser light: the output wavelength (λ) can be varied in the range of 250–4450 nm. For the PL measurement λ is tuned to 532 nm (green) in order to induce one-photon band-to-band excitation (E_g ~ 2.1 eV) with an input pulse energy of 20 μJ. The PL intensity is recorded as a function of wavelength using a charge couple device (CCD) camera. For NLO experiments the incident beam is more tightly focused on the sample with λ being tuned to 1200 nm. We measure the corresponding second harmonic generation (SHG) and third harmonic generation (THG) using the same collection apparatus with a 30 s collection time.

3 Results and discussion

3.1 Growth and morphological control of α-Fe_2O_3 nanowires and nanoblades

Sandblasting is a common mechanical procedure providing repeated impacts on a surface at a high speed and is widely used in metal and alloy treatments. Sand spheres of specific diameters are propelled through a pressurized gun and hit the surface of the metal. The sandblasting can generate compressive residual stresses and high-density dislocations in the target substrate, resulting in increased surface roughness and cracking.[14] Fig. 1(A) shows the surface roughness of the Fe substrates with different sandblasting durations. Clearly, the surface roughness of the Fe substrates increases with increasing the sandblasting time. The inset images are optical profiler 3D surface morphologies of the iron substrates being sandblasted for 0 s (without sandblasting), 3 s, and 9 s, where the surface roughness is increased from ~0.19 μm to 0.62 μm, and then to 2 μm. Fig. 1(B) shows a 3D profile surface image of a single crater formed from the sandblasting. The diameter of the crater is about 200 μm with a ramp area, which corresponds well with the round shape and the diameter range of the spherical glass beads used for the sandblasting. The different surface areas across the crater experience different levels of deformation, as expected from the different stresses exerted during sandblasting. The ramp area experiences more deformation than the

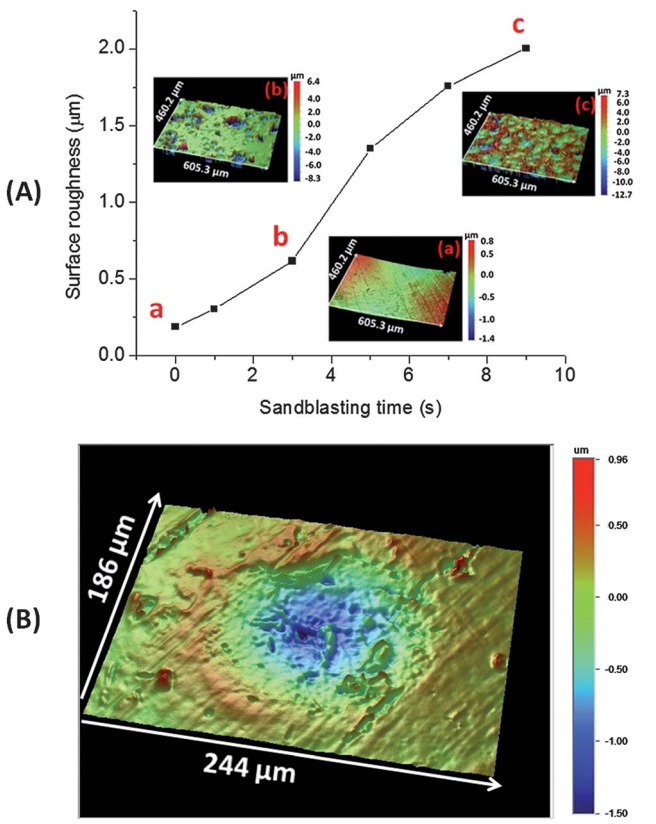

Fig. 1 (A) Surface roughness Ra *vs.* sandblasting time. (a), (b), and (c): 3D surface images taken by profilometer showing the surface morphology of the samples being sandblasted for 0 s, 3 s, and 9 s, respectively. (B) 3D profile image of a single crater formed by sandblasting.

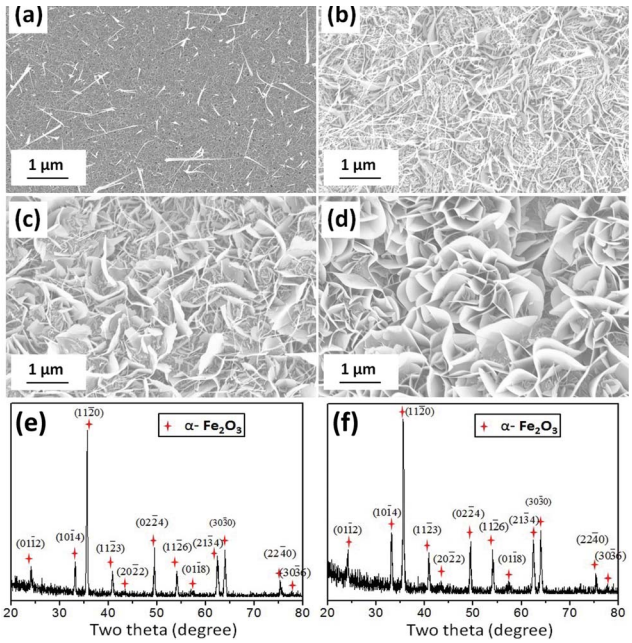

Fig. 2 SEM micrographs of the surface morphology of oxidized Fe substrates sandblasted for (a) 0 s; (b) 5 s; (c) 7 s: (d) 9 s and (e) and (f) are the XRD patterns obtained from (a) and (d), respectively.

rim area but less deformation compared to the bottom area because the ramp area suffers more stress during sandblasting than the rim area but less stress than the crater bottom.

Fig. 2 shows representative SEM images of the surface morphology of the Fe substrates oxidized at the oxygen pressure of 300 mbar and 600 °C for 1 h. Fig. 2(a) is from the flat substrate and Fig. 2(b–d) correspond to the samples which are sandblasted for 5 s, 7 s, and 9 s, respectively. It can be seen that oxidation of the flat Fe sample results in the formation of nanowires with a relatively low surface density. With increasing the sandblasting time to 5 s, the surface density of nanowires increases significantly and nanoblades also start to form. With increasing the sandblasting time to 7 s, the nanowire density starts to decrease while the density of nanoblades continues to increase. On the surface of the Fe sample being sandblasted for 9 s, the entire surface is covered by a high density of nanoblades with almost no nanowire formation. These SEM observations reveal that the flat or slightly sandblasted Fe surface is dominated by the growth of nanowires while the highly roughened surface is dominated by the nanoblade formation. The growth of both nanowires and nanoblades occurs on the surfaces between the two extreme conditions. Fig. 2(e and f) show XRD patterns obtained from as-prepared nanowire and nanoblade samples shown in Fig. 2(a and d), both of which match well with the rhombohedral α-Fe_2O_3 structure. The XRD patterns show that the $(11\bar{2}0)$ peak has a much stronger intensity than other peaks, suggesting that both nanowires and nanoblades grow preferentially along the $[11\bar{2}0]$ direction.

To confirm that such a morphology transition is caused by the enhanced surface roughness, we examine the oxide growth morphology around individual craters generated by sandblasting. Fig. 3 shows a typical single crater formed on a Fe substrate that is sandblasted for 1 s and oxidized for 1 h at 600 °C. As shown by the low-magnification SEM image in Fig. 3(a), the crater has a diameter of ~230 μm, which suggests that the oxidation results in no noticeable change in the shape and size of the crater compared to Fig. 1(B). High-magnification SEM examination reveals that these different surface areas (as marked by b–f in Fig. 3(a)) show different oxide growth morphologies. Fig. 3(b) shows that the flat surface region outside of the crater (*i.e.*, region b shown in Fig. 3(a)) is covered by nanowires with an average length of about 1 μm, which is similar to the case obtained by oxidation of the flat sample without experiencing sandblasting (*i.e.*, Fig. 2(a)). Fig. 3(c) is an SEM image from the crater rim region, which shows that the rim area is covered by nanowires with a higher surface density and longer length. Fig. 3(d) shows the ramp area of the crater, where the density of nanowires is further increased as compared to areas b and c marked in Fig. 3(a). In the area e, both nanowires and nanoblades are visible, where nanoblades are about 1 μm wide, 500 nm high, and 50 nm thick. Fig. 3(f) is from the crater bottom, where large and wide nanoblades are formed. The above observations reveal clearly that the nanowire growth is promoted successively from the outside flat area to the

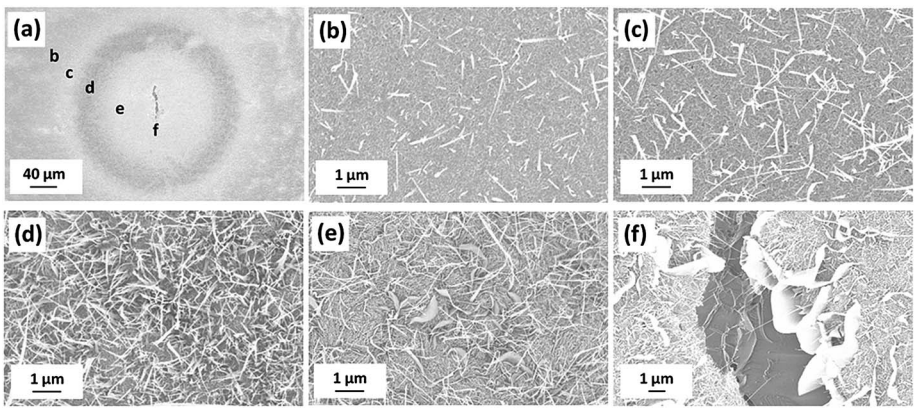

Fig. 3 Typical SEM images of an oxidized Fe sample with individual craters produced by sandblasting for 1 s before the oxidation: (a) a single crater at low magnification and (b–f) the morphology of the areas marked in (a).

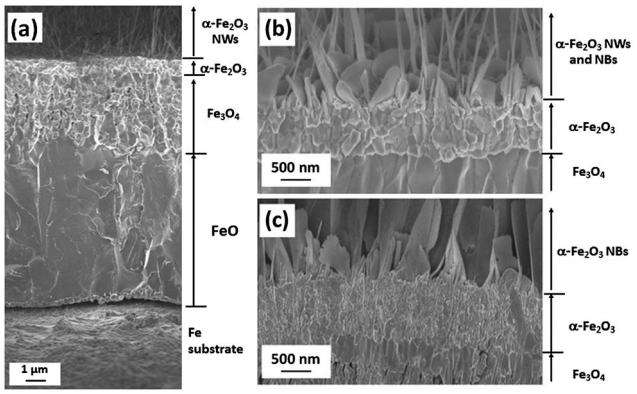

Fig. 4 Interface SEM images showing the Fe_2O_3 morphological transformation from the growth of nanowires to nanoblades by increasing the sandblasting time: (a) flat sample at low magnification showing the growth of a three-layered oxide structure of FeO/Fe_3O_4/Fe_2O_3 with the growth of α-Fe_2O_3 nanowires on the outer α-Fe_2O_3 layer; (b) the growth of both α-Fe_2O_3 nanowires and nanoblades for the Fe sample sandblasted for 5 s and (c) the growth of α-Fe_2O_3 nanoblades for the Fe sample sandblasted for 9 s.

rim region and to the inner ramp area and then suppressed in the crater bottom area while the formation of nanoblades is promoted gradually from the inner ramp area to the crater bottom. For the samples being sandblasted for a longer time, more craters are created, but each crater shows the similar trend. The prolonged sandblasting results in significant overlapping of craters, and the entire surface is thus dominated by nanoblade growth, as shown in Fig. 2(d).

Fig. 4(a) shows a cross-sectional SEM image of a flat Fe substrate oxidized at 600 °C. Three oxide layers (Fe_2O_3/Fe_3O_4/FeO/Fe) are visible with a thick inner FeO layer (~8 μm) in contact with the Fe substrate, an intermediate Fe_3O_4 layer (~4 μm), and a thin outer α-Fe_2O_3 layer (~650 nm thick) on which α-Fe_2O_3 nanowires grow. The phases of the different oxide layers can be confirmed by measuring the oxide compositions using X-ray energy dispersion spectroscopy (EDS) in conjunction with the SEM observation of the cross-section of the oxidized Fe samples, as shown in our earlier work.[19] In addition, the phase of the underlying oxide layers was also confirmed by the TEM electron diffraction pattern as shown later in Fig. 6(d). A similar layered oxide structure is observed from oxidation of sandblasted Fe samples, however, the interface between the FeO layer and the sandblasted Fe substrate is rough and varies dramatically across the FeO/Fe interface area due to the large surface roughness caused by sandblasting. Shown in Fig. 4(b and c) are interface SEM images obtained from the oxidized Fe samples being sandblasted for 5 s and 9 s, respectively, *i.e.*, corresponding to the samples shown in Fig. 2(b) and (d). The interface images further confirm the surface morphology transformation from the growth of nanowires to nanoblades upon increasing the sandblasting time. Close examination of the different areas indicates that the bottom FeO layer contains large grains and the intermediate Fe_3O_4 layer is composed of coarse columnar grains whereas the outer α-Fe_2O_3 layer consists of considerably fine grains.

Fig. 5(a) is a cross-sectional SEM image showing the root region of the Fe_2O_3 nanowire growth. It can be seen that nanowires grow directly on the underlying Fe_2O_3 grains. This can be further confirmed by the inset SEM image of the initial growth morphology of a Fe_2O_3 nanowire, which reveals that the Fe_2O_3 nanowire is formed on top of the underlying Fe_2O_3 grain. Fig. 5(b) is an HRTEM image, which shows that the nanowire has a bi-crystal structure. The lattice image reveals that the two sides of the nanowire have different crystal orientations but share the same growth direction (*i.e.*, length direction) along [11$\bar{2}$0], as shown in the inset bright-field TEM of Fig. 5(b). The origin resulting in forming a bi-crystal structure in the nanowire can be ascribed to the side facets of underlying Fe_2O_3 grains, on which Fe_2O_3 nanowires nucleate and grow. The crystals grown on the side facets of a Fe_2O_3 grain naturally merge at the grain apex and form a twin structure starting from the grain top and continuing into the nanowire along the axial direction.

Fig. 6(a) is a cross-sectional SEM image of the nanoblade growth morphology. Different from the nanowire growth occurring directly on top of Fe_2O_3 grains, the nanoblade root can be traced to the Fe_2O_3/Fe_3O_4 interface. It can be seen that the nanoblade is formed *via* merging of two thin Fe_2O_3 grains and the thickness becomes gradually thinner from the root region to the top end. The merged grain boundary of the nanoblade starts from the Fe_2O_3/Fe_3O_4 interface and continues into the extruding portion above the Fe_2O_3 layer. A cross-sectional TEM specimen is also made to examine the root region of the nanoblades formed from oxidation of the sandblasted Fe. Fig. 6(b) is a bright-field TEM image obtained from the Fe_2O_3/Fe_3O_4 region. Consistent with the SEM observation, it is visible that the nanoblade is rooted at the Fe_2O_3/Fe_3O_4 interface and the merging boundary runs through the entire nanoblade, confirming the growth feature revealed from the SEM observation shown in Fig. 6(a). Fig. 6(c) is an HRTEM image taken from the nanoblade marked by the dashed black rectangle in Fig. 6(b), which shows clearly the presence of the boundary formed from the merged grains. Fig. 6(d) is a typical selected area electron diffraction (SAED) pattern obtained from the large Fe_3O_4 grain underneath the Fe_2O_3 layer as shown in Fig. 6(b), and the diffraction pattern can be indexed with the cubic Fe_3O_4 structure.

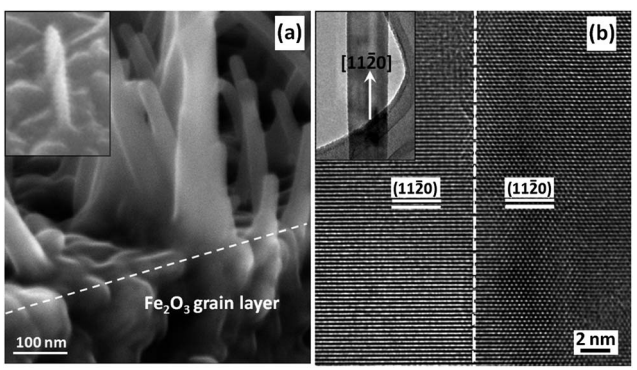

Fig. 5 (a) Typical cross-sectional SEM image shows that hematite nanowires are formed on the underlying Fe_2O_3 layer; the inset SEM image shows the growth of an initially formed nanowire, revealing that the nanowire is formed on top of a single Fe_2O_3 grain and (b) HRTEM image revealing the bi-crystal structure of the Fe_2O_3 nanowire. The nanowire growth direction is along [11$\bar{2}$0] as shown in the inset TEM image.

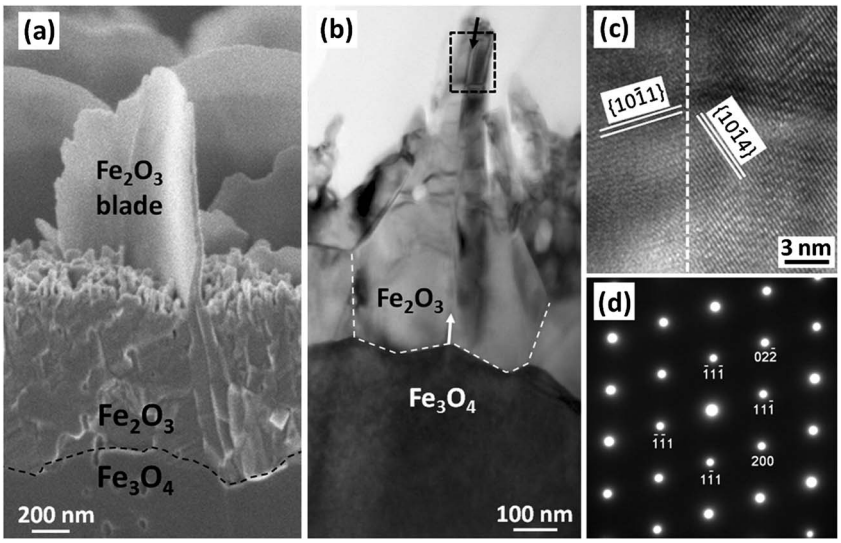

Fig. 6 (a) Typical cross-sectional SEM image reveals that nanoblades are originated from the Fe_2O_3/Fe_3O_4 interface with a visible merged grain boundary starting from the Fe_2O_3/Fe_3O_4 interface through the entire nanoblade; (b) cross-sectional bright-field TEM image further confirms that the nanoblades are rooted from the Fe_2O_3/Fe_3O_4 interface and the boundary formed by merging Fe_2O_3 grains runs through the entire nanoblade; (c) HRTEM image recorded from the rectangle area marked in (b) confirms the existence of the merged boundary in the nanoblade and (d) SAED pattern from the underlying Fe_3O_4 grain shown in (b) reveals the single crystal structure of the large grain.

According to the iron–oxygen phase diagram,[15] three iron oxides, FeO, Fe_3O_4, and α-Fe_2O_3, form upon oxidation. Oxidation of Fe at 600 °C develops a $Fe_2O_3/Fe_3O_4/FeO/Fe$ layered structure with the FeO layer next to the Fe substrate and the Fe_2O_3 layer on top, as shown in Fig. 4(a). Such oxide layering is governed by the Fe and oxygen gas equilibrium conditions with the stability of Fe_2O_3 > Fe_3O_4 > FeO under the oxidation condition employed in the present study. The layered oxide growth is driven by chemical potential gradient across the oxide layers due to many orders of magnitude in oxygen gas pressure between Fe/FeO and Fe_2O_3/O_2 interfaces. Fe_2O_3 forms first on the bare Fe substrate upon oxidation under the high oxygen pressure. The thickening of the Fe_2O_3 layer results in a significant drop in the oxygen pressure at the buried Fe_2O_3/Fe interface, for which the formation of Fe_3O_4 becomes more favorable and the inner portion of the Fe_2O_3 layer is thus reduced to Fe_3O_4 at the Fe_2O_3/Fe interface. This results in the formation of two new interfaces, *i.e.*, the Fe_2O_3/Fe_3O_4 and Fe_3O_4/Fe. Further drop in the oxygen pressure at the Fe_3O_4/Fe interface for continued oxidation makes FeO more stable and the Fe_3O_4 phase adjacent to the Fe_3O_4/Fe interface is thus reduced to FeO at the interface, resulting in the observed $Fe_2O_3/Fe_3O_4/FeO/Fe$ layered structure as shown in Fig. 4(a).

Based on our experimental observations and the layered-oxide growth described above, the effects of surface sandblasting on the Fe_2O_3 morphological transformation are schematically shown in Fig. 7. Oxidation of many metals including Fe at high temperature proceeds *via* nucleation, growth, and coalescence of oxide nanoislands, which can be significantly influenced by the surface conditions of the metal substrate.[16] During the early stages of oxidation of Fe, it first forms Fe_2O_3 nuclei under the high oxygen pressure and temperature.[17] As oxidation continues, Fe_2O_3 nuclei impinge with each other,

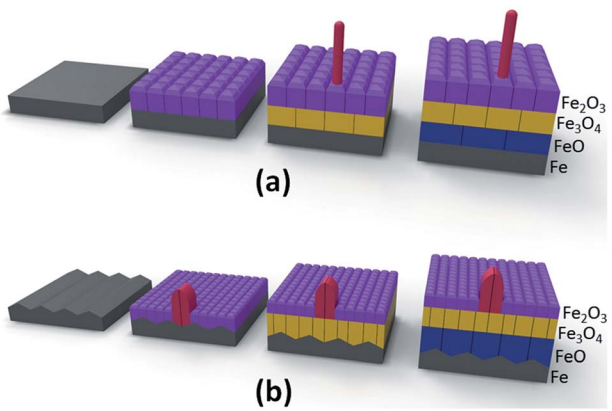

Fig. 7 Schematics showing the growth of Fe_2O_3 nanowires and nanoblades: (a) oxidation of a flat Fe surface: oxide nucleation and growth on Fe_2O_3 grains results in Fe_2O_3 nanowire growth; (b) oxidation of a sandblasted Fe surface: merging Fe_2O_3 grains nucleated and grown on the adjacent areas of a Fe surface trench produced by sandblasting results in a Fe_2O_3 nanoblade growth with a bi-crystal structure. For both cases, the phase of Fe_2O_3 is formed first and is subsequently transformed to Fe_3O_4 at the Fe_2O_3/Fe interface and then to FeO at the Fe_3O_4/Fe interface due to the oxygen pressure drop across the interfaces.

resulting in fine grains in the coalesced Fe_2O_3 layer.[18] The significant drop in oxygen pressure at the Fe_2O_3/Fe interface leads to Fe_3O_4 formation at the Fe_2O_3/Fe interface and then FeO formation at the Fe_3O_4/Fe interface. The Fe_2O_3/Fe_3O_4 interfacial reaction for this phase transition generates interfacial stress due to the molar volume difference between the two oxides, which drives Fe_2O_3 nanowire formation on top of Fe_2O_3 grains to accompany the relaxation of interfacial stress by grain boundary diffusion, as shown in our previous work.[19] Since grains typically show different surface facets, crystals nucleated on the side facets of a grain grow and merge at the grain top to

form a bi-crystal structure. Such a process of the nanowire formation is schematically shown in Fig. 7(a).

However, prolonged sandblasting onto the Fe substrate results in significant plastic deformation and even cracking, particularly at the bottom of craters which experiences larger stress than the surrounding areas. This can be seen evidently from Fig. 3(a), which shows the formation of a crack at the crater bottom. A higher density of nanoblades at the crater bottom indicates that these deformed surface areas are energetically more favorable for nucleation of Fe_2O_3 grains, as shown schematically in Fig. 7(b). Oxide grains nucleated on the adjacent faces of the deformed regions grow and merge to form a bi-crystal, resulting in the morphology of nanoblades, which is correlated with the geometry of surface deformation caused by sandblasting. The nanoblades grow at the tip *via* fast diffusion of Fe atoms through the merged planar grain boundary which leads to the platelet growth with the wide and thin blade geometry. Initially, Fe cations supporting the nanoblade growth are directly from the underlying Fe substrate through the internal grain boundary formed by merging Fe_2O_3 grains. With continued oxidation that leads to the formation of the thermodynamically more stable phases of Fe_3O_4 and FeO at the inner regions, the root region of the nanoblade is thus transformed to Fe_3O_4 to accompany the layered oxide growth. The process of the nanoblade formation is shown schematically in Fig. 7(b). The oxide growth by this mechanism results in direct contact of Fe_2O_3 nanoblades with the Fe_2O_3/Fe_3O_4 interface, and this is consistent with our SEM and TEM observations, as shown in Fig. 6. It becomes evident that the formation of nanowires and nanoblades has their different origins, *i.e.*, nanowires are grown on top of Fe_2O_3 grains while nanoblades are formed on the trench areas of the Fe substrate that are produced by sandblasting.

3.2 Optical properties of α-Fe_2O_3 nanowires and nanoblades

To examine the effect of the morphology–property correlations, we perform both PL and NLO experiments on several hematite nanoblade and nanowire samples at room temperature. Fig. 8 shows the time-integrated PL from a representative nanoblade sample (red trace) and a nanowire sample (blue trace), respectively, obtained under the same experimental conditions; the green line indicates the laser excitation (532 nm). The onset of the PL occurs below the bandgap (E_g ~2.1 eV), which extends all the way down to a near-infrared (IR) range with the maximum around 670 nm. This broad PL spectrum indicates that it arises due to electron–hole recombination.[20] The overall PL trend for both types of hematite is rather similar but the corresponding PL intensity is significantly more intense for the nanoblade sample. Although the PL intensities for both the nanowire and nanoblade samples are quite low, the measurable PL from our nanostructured α-Fe_2O_3 samples is interesting because it is well known that α-Fe_2O_3 in the bulk does not show any photoluminescence.[21] Due to the small exciton Bohr radius in α-Fe_2O_3, it has been suggested that the changes of the band structure caused by the size reduction is not evident, but the surface effect become dominant in determining the properties

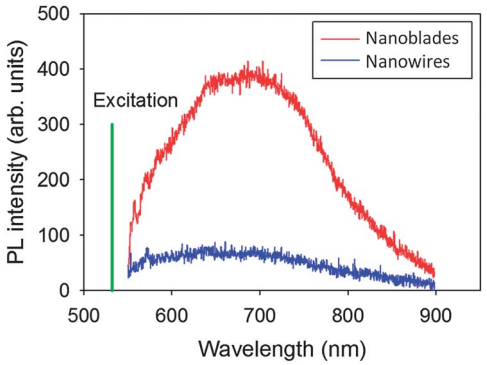

Fig. 8 Room-temperature time-integrated PL spectra obtained from Fe_2O_3 nanoblades (red traces) and Fe_2O_3 nanowires (blue trace), respectively. The laser excitation is indicated by the green line.

of nanostructured α-Fe_2O_3.[21] Indeed, our PL measurements showed that the nanoblade samples have stronger PL compared to the nanowire samples (Fig. 8). This is presumably due to the more significantly extended surface area associated with the nanoblade morphology compared to that for the nanowire morphology, which thus results in more effective illumination by the incident laser beam.

We now present NLO properties of the samples based on the SHG and THG responses at $\lambda = 1200$ nm. Note that this λ is chosen to avoid any possible two-photon absorption of the input beam. When an intense light enters an NLO medium, the dielectric polarization $P(t)$ of the medium responds nonlinearly to the electric field of the incident light $E(t)$ at time t and can be written by

$$P(t) = \varepsilon_0[\chi^{(1)} E(t) + \chi^{(2)} E^2(t) + \chi^{(3)} E^3(t) + \ldots] \quad (1)$$

where ε_0 is the vacuum dielectric constant and the coefficients $\chi^{(n)}$ are the n-th order susceptibilities of the NLO material. Although eqn (1) is written in its simplest form, it is important to note that $\chi^{(n)}$ are generally tensors operating on each of the components of the electric field.

Second harmonic generation (SHG) arises from the second term and is nonzero only in crystals which lack *inversion symmetry*. This results in the phenomenon of frequency doubling, where an input pump wave generates a wave with twice the frequency, and therefore half the wavelength, inside the NLO material. Therefore, the corresponding SHG wavelength is (1200 nm)/2 = 600 nm for our experiment. Similarly, third harmonic generation (THG) is the frequency tripling process and can be achieved with the third-order nonlinearity $\chi^{(3)}$ in eqn (1). The corresponding THG wavelength is (1200 nm)/3 = 400 nm for our experiment. Unlike SHG that requires noncentrosymmetry, THG essentially occurs in every material.

Fig. 9(a) plots the SHG photon number measured from a Fe_2O_3 nanowire sample at $\lambda = 1200$ nm. It can be seen that the sample exhibits some weak SHG. This further confirms that the sample is α-Fe_2O_3 (crystal structure: rhombohedral) rather than the γ-phase which is cubic and no SHG is thus anticipated. The corresponding THG photon number obtained from the Fe_2O_3 nanowire sample under the same experimental condition is

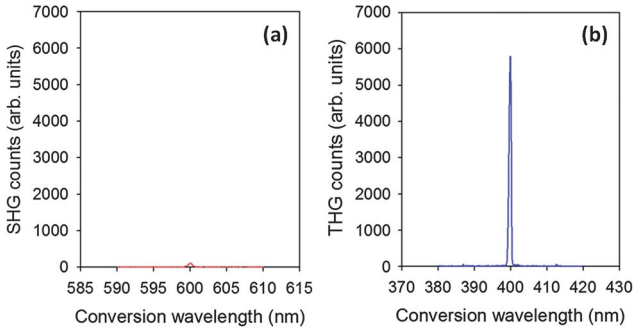

Fig. 9 (a) SHG and (b) THG from the Fe_2O_3 nanowire sample when λ is set to 1200 nm, respectively. However, no harmonic signals are observed from the Fe_2O_3 nanoblade samples.

plotted in Fig. 9(b). It is quite surprising that the THG is much stronger than the SHG considering that THG is a higher-order process. This unusual case might occur due to the relatively random orientations of nanowires that tend to cancel the overall SHG dipole moments, whereas the odd-parity THG polarization persists in this random structure.[22] We do not see any measurable SHG and THG signal from all the nanoblade samples (4 samples examined) under the same experimental conditions. This implies that NLO properties can strongly depend on the structural configuration of hematite. In fact, the NLO coefficients tend to increase for a lower-dimensional sample geometry (like nanowires) due to the contribution from a local enhancement of the field.[23]

4 Conclusion

In summary, we have demonstrated an efficient approach for the selective growth of hematite nanowires and nanoblades during thermal oxidation of iron. By exerting sandblasting onto Fe substrates, we find that an initial increase in the surface roughness can promote α-Fe_2O_3 nanowire growth while further increase in surface roughness leads to the transformation from the growth of α-Fe_2O_3 nanowires to α-Fe_2O_3 nanoblades. We show that such a growth morphology transformation is driven by the effect of sandblasting which results in surface deformation, where nanoblades nucleate and grow on trench areas of the deformed regions. It is observed that PL and NLO properties show clear dependence on the growth morphologies of the nanostructured hematite. Due to the simplicity and widespread availability of sandblasting, it is expected that this approach can be easily extended to other metals and alloys for producing oxide nanostructures with hybrid growth morphologies.

Acknowledgements

This work was supported by the National Science Foundation under the Grant no. CMMI-0825737. We thank David Richner for access to the sandblasting equipment. Q. Wang would like to thank the financial support from the Natural Science Foundation for Outstanding Young Scientists in Shandong Province, China (Grant no: JQ201002) and Taishan Scholar Program.

References

1 Z. L. Wang, *J. Phys.: Condens. Matter*, 2004, **16**, R829; J. G. Lu, P. Chang and Z. Fan, *Mater. Sci. Eng., R*, 2006, **52**, 49; C. M. Lieber and Z. L. Wang, *MRS Bull.*, 2007, **32**, 99.
2 Z. L. Wang, *Adv. Mater.*, 2003, **15**, 432; E. Comini, C. Baratto, G. Faglia, M. Ferroni, A. Vomiero and G. Sberveglieri, *Prog. Mater. Sci.*, 2009, **54**, 1.
3 Y. Zhu, C. H. Sow, T. Yu, Q. Zhao, P. Li, Z. Shen, D. Yu and J. T. L. Thong, *Adv. Funct. Mater.*, 2006, **16**, 2415; Z. Dai, Z. Pan and Z. Wang, *Adv. Funct. Mater.*, 2003, **13**, 9; M. L. Zhong, D. C. Zeng, Z. W. Liu, H. Y. Yu, X. C. Zhong and W. Q. Qiu, *Acta Mater.*, 2010, **58**, 5926; G. W. Zhou, L. Wang, R. C. Birtcher, P. M. Baldo, J. E. Pearson, J. C. Yang and J. A. Eastman, *Phys. Rev. Lett.*, 2006, **96**; G. W. Zhou, W. S. Slaughter and J. C. Yang, *Phys. Rev. Lett.*, 2005, **94**; G. W. Zhou and J. C. Yang, *Phys. Rev. Lett.*, 2002, **89**.
4 Y. Zheng, Y. Cheng, Y. Wang, F. Bao, L. Zhou, X. Wei, Y. Zhang and Q. Zheng, *J. Phys. Chem. B*, 2006, **110**, 3093.
5 J. Chen, L. Xu, W. Li and X. Gou, *Adv. Mater.*, 2005, **17**, 582.
6 Y. S. Hu, A. Kleiman-Shwarsctein, A. J. Forman, D. Hazen, J. N. Park and E. W. McFarland, *Chem. Mater.*, 2008, **20**, 3803.
7 D. K. Zhong, J. Sun, H. Inumaru and D. R. Gamelin, *J. Am. Chem. Soc.*, 2009, **131**, 6086.
8 L.-C. Hsu, Y.-Y. Li, C.-G. Lo, C.-W. Huang and G. Chern, *J. Phys. D: Appl. Phys.*, 2008, **41**, 185003.
9 S. W. Cao and Y. J. Zhu, *J. Phys. Chem. C*, 2008, **112**, 6253.
10 M. Mahmoudi, A. S. Milani and P. Stroeve, *Int. J. Biomed. Nanosci. Nanotechnol.*, 2010, **1**, 164.
11 Q. Han, Z. Liu, Y. Xu, Z. Chen, T. Wang and H. Zhang, *J. Phys. Chem. C*, 2007, **111**, 5034.
12 A. G. Nasibulin, S. Rackauskas, H. Jiang, Y. Tian, P. R. Mudimela, S. D. Shandakov, L. I. Nasibulina, S. Jani and E. I. Kauppinen, *Nano Res.*, 2010, **2**, 373; L. Yuan, Q. Jiang, J. Wang and G. Zhou, *J. Mater. Res.*, 2012, **27**, 1014; X. Wen, S. Wang, Y. Ding, Z. L. Wang and S. Yang, *J. Phys. Chem. B*, 2005, 215; U. Cvelbar, Z. Chen, M. K. Sunkara and M. Mozetič, *Small*, 2008, **4**, 1610; Z. Chen, U. Cvelbar, M. Mozetic, J. He and M. K. Sunkara, *Chem. Mater.*, 2008, **20**, 3224.
13 M. A. Lukowski and S. Jin, *J. Phys. Chem. C*, 2011, **115**, 12388.
14 X. S. Guan, Z. F. Dong and D. Y. Li, *Nanotechnology*, 2005, **16**, 2963; I. Nikitin, I. Altenberger, H. J. Maier and B. Scholtes, *Mater. Sci. Eng., A*, 2005, **403**, 318.
15 N. Birks, G. H. Meier and F. S. Pettit, *Introduction to the high temperature oxidation of metals*, Cambridge University Press, Cambridge, 2006.
16 G. W. Zhou and J. C. Yang, *Surf. Sci.*, 2004, **559**, 100.
17 B. Pujilaksono, T. Jonsson, M. Halvarsson, J.-E. Svensson and L.-G. Johansson, *Corros. Sci.*, 2010, **52**, 1560; N. Bertrand, C. Desgranges, D. Poquillon, M. C. Lafont and D. Monceau, *Oxid. Met.*, 2009, **73**, 139.
18 L. Yuan and G. Zhou, *J. Electrochem. Soc.*, 2012, **159**, C1; R. Mema, L. Yuan, Q. T. Du, Y. Q. Wang and G. W. Zhou, *Chem. Phys. Lett.*, 2011, **512**, 87.
19 L. Yuan, Y. Wang, R. Cai, Q. Jiang, J. Wang, B. Li, A. Sharma and G. Zhou, *J. Mater. Sci. Eng. B*, 2012, 177–327; L. Yuan,

Y. Q. Wang, R. Mema and G. W. Zhou, *Acta Mater.*, 2011, **59**, 2491.
20 T. Ito, H. Yamaguchi, K. Okabe and T. Masumi, *J. Mater. Sci.*, 1998, **33**, 3555.
21 H. S. Fei, X. C. Ai, M. Y. Gao, Y. Q. Yang, T. Q. Zhang and J. C. Shen, *J. Lumin.*, 1996, **66/67**, 345; B. S. Zou and V. Volkov, *J. Phys. Chem. Solids*, 2000, **61**, 757.
22 J. Jang, S. Park, N. Frazer, J. Ketterson, S. Lee, B. Roy and J. Cho, *Solid State Commun.*, 2012, **152**, 1241.
23 M. Fu, H. Long, K. Wang, G. Yang and P. Lu, *Thin Solid Films*, 2011, **519**, 6557; R. Ganeev and A. Ryasnyansky, *Phys. Status Solidi A*, 2005, **202**, 120; Y. Deng, Y. Du, M. Zhang, J. Han and Z. Yin, *Solid State Commun.*, 2005, **135**, 221.

